Transition from nonvolatile bipolar memory switching to bidirectional threshold switching in layered MoO_3 nanobelts

Huiying Du[1], Jinghong Chen[1], Meilin Tu[1], Songwen Luo[1], Shangdong Li[2], Shuoguo Yuan[3], Tianxun Gong[2], Wen Huang[2], Wenjing Jie[1]* and Jianhua Hao[3]*

[1]College of Chemistry and Materials Science, Sichuan Normal University, Chengdu, 610066, China

[2]State Key Laboratory of Electronic Thin Films and Integrated Devices, School of electronic Science and Engineering, University of Electronic Science and Technology of China, Chengdu, 610054, China

[3]Department of Applied Physics, The Hong Kong Polytechnic University, Hung Hom, Kowloon, Hong Kong, China

***Corresponding authors:**

Wenjing Jie, Email: wenjing.jie@sicnu.edu.cn

Jianhua Hao, Email: jh.hao@polyu.edu.hk

ABSTRACT

The resistive switching (RS) can be divided into two categories, namely the nonvolatile memory switching and volatile threshold switching, depending on the volatility. MoO_3 is one type of versatile transition metal oxides with high work function, large electron affinity and wide band gap for potential applications in electronics, optoelectronics, batteries and electrochromic devices. Herein, we report the transition from the nonvolatile memory to the volatile threshold switching in single MoO_3 nanobelts simply by changing the electrodes from Au to Ag. The one-dimensional (1D) α-MoO_3 nanobelts are synthesized by hydrothermal method and annealed under different atmospheres to adjust the concentration of oxygen vacancies. The prepared single MoO_3 nanobelt is used to serve as the RS layer to construct the lateral two-terminal RS devices. By using Au as the electrodes, the MoO_3 nanobelts show the typical nonvolatile bipolar memory RS behaviors. On the other hand, bidirectional threshold RS properties can be achieved by employing Ag as the electrodes due to large contact resistance between Ag and MoO_3. More importantly, the threshold RS performance is significantly enhanced by annealing the nanobelts in N_2. The ON/OFF current ratio is increased up to 3×10^5 while the threshold voltage is decreased down to 0.75 V. These results demonstrate the diverse RS behaviors in single 1D MoO_3 nanobelts and potential applications in volatile and non-volatile switching devices. In addition, the finding provides guidelines for improvement and/or alternation the RS behaviors through defect engineering and/or device modification in the multifunctional emerging devices.

KEYWORDS: 1D materials; MoO_3 nanobelts; resistive switching; nonvolatile; threshold switching

INTRODUCTION

Resistive switching (RS) has drawn considerable attention owing to its promising applications in memory devices as a suitable alternative to Si-based memories especially since this century. The memristor shows versatile application ranging from non-volatile memory to logic device and computing as well as recently developed multifunctional synaptic neurons.[1-4] The memristor is typically a two-terminal device with a metal/RS layer/metal sandwich structure. Accordingly, the RS layer is in the form of thin film sandwiched with the top and bottom electrodes. Thanks to the harvest in modern nanotechnology, a number of nanomaterials have been used to work as the RS layer in various memristors, from zero-dimensional nanoparticles, to one-dimensional (1D) nanowires (NWs) and recently widely studied two-dimensional (2D) nanosheets.[5-9] For 1D nanomaterials, typically, the RS devices can be realized by using as grown NW arrays or randomly oriented NWs networks based on the metal/NWs/metal sandwiched vertical structure.[10-12] Besides, the RS devices can also be achieved by using single NWs connecting two metal electrodes in a planar structure, where a unique 1D platform can be provided for nanoscale controlling and improving the switching behaviors as well as exploring and understanding the switching mechanism. However, much attention was put on investigating the overall RS behaviors of the 1D NWs.[13] While, only a few researches focused on the RS performance of the individual 1D NWs through micromanipulator.[14] Since 2008, a series of individual 1D NWs have been employed in RS devices, such as ZnO, NiO, WO_3, TiO_2, CuO and so on.[15-17] Among them, MoO_3 is one type of versatile transition metal oxides with high work function, large electron affinity and wide band gap larger than 3 eV.[18-20] Thus, MoO_3 is a technologically relevant semiconductor to serve as the excellent hole dopant owing to its large electron affinity. Furthermore, it is almost transparent to visible light due to its wide bandgap. Besides, MoO_3 nanobelts with Au electrodes were reported to exhibit unipolar RS behaviors with ~10^3 ON/OFF current ratio.[21] However, a systematical study of the RS behaviors of 1D MoO_3 nanobelts is still in absence.

To date, diverse RS behaviors have been reported in a series of materials from insulators to semiconductors and from inorganic to organic materials.[22-25] Nonvolatile memory switching (MS) and volatile threshold switching (TS) are two types of widely studied RS phenomena depending on the volatility. In MS devices, both the high resistive state (HRS) and the low resistive state (LRS) can be maintained after removing the external voltage. On the other hand, the TS devices will be back to the HRS without the applied external voltage.[26, 27] The MS is suitable for the non-volatile data storage, computing and synaptic neurons, while the TS can be used as a selector in the crossbar array to suppress sneak path currents.[26] In the real applications of MS devices based crossbar arrays, the sneak path currents from neighboring cells can be formed and severely impede the proper operation of the array during a write or read of a memristor cell.[28] The two-terminal selectors are applicable to addressing the issue in both scalability and 3D stacking of the MS devices.[27,29] Furthermore, the transition between the TS and the MS was previously reported through setting different current limitations.[30-33] Generally, the MS can be obtained by setting a high current limitation while the TS is stimulated by setting a relatively low current limitation. This provides us opportunity to deepen understanding of the physical mechanism of the two types RS behaviors and to achieve multifunctional emerging devices with high performance based on RS devices.

Herein, we demonstrate a transition from the nonvolatile MS to the volatile TS by using individual MoO_3 nanobelts as the RS layer. 1D layered α-MoO_3 nanobelts were prepared by a hydrothermal method. A "dry" approach was employed to fabricate the RS device based on single MoO_3 nanobelt, avoiding interaction of the prepared nanobelts with any chemical solvents during the individual nanobelt transferring and electrodes deposition processes. A transition from the nonvolatile MS to the volatile TS in single MoO_3 nanobelts can be observed in our experiments. By using Au as the electrodes, the MoO_3 nanobelts show the typical nonvolatile bipolar MS behaviors, while, bidirectional TS properties can be achieved by employing Ag as the electrodes.

RESULTS AND DISCUSSION

The 1D MoO_3 nanobelts were synthesized by a hydrothermal method. X-ray diffraction (XRD) was used to determine the crystal structure of the prepared MoO_3 nanobelts. As shown in Figure 1a, the strong diffraction peaks are located at 12.780°, 25.699°, and 38.979°, corresponding to the (020), (040) and (060) planes of MoO_3, respectively. All the diffraction peaks are well in accordance with the orthorhombic structure of MoO_3 (Joint Committee on Powder Diffraction Standards (JCPDS) NO.05-0508, a=0.3962 nm, b=1.3858 nm, c=0.3697 nm, space group *Pbnm*, as seen by the black line in Figure 1a), suggesting the 1D nanobelts are well prepared. Raman spectroscopy was used to further distinguish microstructure of the 1D nanobelts.[34] As shown in Figure 1b, Raman feature peaks are situated at 284.2, 337.3, 377.9, 665.4, 818.7, 996.1 cm^{-1}, suggesting the prepared nanobelt is α-MoO_3.[35] To be more specific, the peak at 284.2 cm^{-1} (B_{2g}, $_{3g}$) suggests the rocking mode of the double bond O=Mo=O. The Raman peaks at 337.3 cm^{-1} (B_{1g}) and 377.9 cm^{-1} (A_g) represent a vibration bending mode of Mo_3-O and Mo=O, respectively. The peak at 665.4 cm^{-1} (B_{2g}, B_{3g}) is attributed to Mo_3-O stretching mode of the triple-coordinating oxygen atom, owing to the co-edge oxygen atoms shared by three adjacent octahedrons. The Raman peak at 818.7 cm^{-1} (A_g, B_{1g}) is assigned to the double coordination bridge oxygen (Mo_2-O) stretching mode, caused by the angular shared oxygen atoms shared by two octahedrons. The band locating at 996.1 cm^{-1} (A_g, B_{1g}) is attributed to the terminal oxygen (Mo^{6+}=O) tensile mode of the unique molybdenum oxygen bond (Mo = O), revealing an unshared oxygen. The XRD and Raman data can well confirm the prepared nanobelt is orthorhombic α-MoO_3 with layered structure. The morphology of the MoO_3 nanobelts was characterized by high-resolution transmission electron microscope (HRTEM), as shown in Figure 1c and d. The nanobelts have a length in the range of 80-110 μm and a width of ~1 μm. HRTEM image indicates that the as-obtained materials have lattice spacings of 3.9 Å and 3.6 Å, corresponding to the (100) and (001) planes, respectively,[36] in accordance with the selected area electron diffraction (SAED) image, as shown in the inset of Figure 1d.

As shown in Figure 2a, the prepared α-MoO_3 has a unique layered structure. The planar unit of α-MoO_3 is made of atomic double layer which composes of the connected twisted MoO_6 octahedra. The layered structure is stacked by weak van der Waals forces, while the interaction between atoms within the bilayer is strong covalent bonding.[37] For device fabrication, we developed a "dry" transferring approach to avoiding any affects from chemical solutions. The MoO_3 nanobelts were transferred onto SiO_2 substrates by using the scotch tape-based mechanical exfoliation method. Through this method, we can successfully obtain individual MoO_3 nanobelts without interaction with any chemical solutions. Then, Au electrodes are deposited through a well-designed shadow mask by sputtering method, as shown in Figure 2b of the schematic of the lateral RS devices. The detailed device fabrication and characterization are described in the experimental section. The scanning electron microscope (SEM) was used to characterize the morphology of MoO_3 nanobelts after transferred onto the SiO_2 substrate (Figure 2c and d). The energy dispersive spectrometer (EDS) confirms that the nanobelts are composed of Mo and O and the atomic ratio is about 1:3 (inset of Figure 2d). The atomic force microscope (AFM) image (Figure 2e) suggests the MoO_3 nanobelt with a thickness of ~70 nm. By considering that the unit layer thickness is ~1.4 nm,[38,39] the prepared MoO_3 nanobelt consists of ~50 atomic layers. The Raman spectroscopy was used to characterize individual of MoO_3 nanobelt after transferring it onto the SiO_2 substrate, as shown in Figure 2f. The observed feature peaks are consistent with those in the Raman spectrum of the MoO_3 powder. The strong peak located at ~520 cm^{-1} is from the underlying SiO_2/Si substrate. All the characterizations suggest that the MoO_3 nanobelt can be well transferred onto SiO_2 substrate by the scotch tape-based mechanical exfoliation method.

Next, we studied the RS properties of single MoO_3 nanobelts based on the planer Au/MoO_3/Au structure. Figure 3a shows the current–voltage (*I*–*V*) characteristics in linear coordinates with the applied external voltage scanned in the sequence of 0 V→+5 V→0 V→–5 V→0 V. The arrows suggest the scanning direction of the applied voltage. The device demonstrates the typical bipolar non-volatile MS behaviors. An electroforming process is required to trigger the device from the HRS to the LRS by applying a positive voltage (10 V) on the Au electrodes, as shown in the inset of Figure 3a. A compliance current (I_{cc}) of 1 mA is set to prevent any dielectric breakdown of the device. The device is initially at the LRS after electroforming, as shown in Figure 3b. The current abruptly decreased from 10^{-4} to 10^{-7} A at ~ 3 V during the positive voltage scan (0 V→ 5 V → 0 V), suggesting the device is switched to the HRS. Then, the HRS can be maintained until the negative voltage is in excess of – 3 V during the negative sweeping (0 V → – 5 V → 0 V). After that, the device changes from HRS into LRS and the LRS can also be maintained at the initial state for the next sweeping loop. The typical nonvolatile RS behaviors can be observed in the Au/MoO_3/Au memristor with the ON/OFF current ratio up to 5.0×10^2 and the switching voltage of ~ 3 V. To understand the RS mechanism, the positive part of the *I*–*V* curve is re-plotted using double-logarithmic coordinates, as shown in Figure 3c. For the LRS, the curve shows the linear relationship, suggesting the formation of conductive filaments of oxygen vacancy between MoO_3 and Au at the LRS. Then the device switches into the HRS, the current dramatically decreased, following the relationship of $I \sim V^a$ ($a > 1$). In addition, the curve follows a linear behavior ($I \sim V$) at the HRS in the range of low voltage ($V < 0.5$ V). It implies the resistance of MoO_3 nanobelts is huge, which is larger than or comparable to the contact resistance between MoO_3 and Au electrode. Furthermore, the electronic structure of Au and MoO_3 is schematically demonstrated in Figure 3d for an in-depth understanding of the metal-semiconductor contact. As a well-known oxide with high work function (Φ, ~ 6.86 eV), MoO_3 possesses a large electron affinity (> 6 eV) and a wide band gap value (> 3 eV).[18-20] Thus, when the metal Au with the work function of 5.1 eV comes in close contact with the MoO_3, non-rectifying junction can be formed. This is also consistent with the linear *I–V* curve at the HRS.

Moreover, it is unusual that an electroforming process triggers the device to the LRS by applying a positive voltage while the subsequent SET process occurs in negative voltages for bipolar non-volatile RS behaviors. As shown in the inset of Figure 3a, the oxygen vacancies are migrated and gathered together to generate conducting filaments in the MoO_3 nanobelt in the forming process,[21,40] inducing the device changing from HRS to LRS. Subsequently, high current density gives rise to the rupture of filaments due to the induced Joule heating, tuning the device from LRS to HRS in the RESET process. It should be noted that a large negative bias voltage is normally needed for the damage of the filaments in bipolar RS by considering an electroforming process is achieved by applying a positive voltage. Herein, we actually achieved unipolar RS behaviors at this stage. Then, the device is changed from the HRS to LRS when the large negative voltage is applied due to the formation of oxygen vacancy filaments. During this stage, the transition from unipolar to bipolar RS can be activated. While, a further bias loop is needed for the completion of the transformation. For a good understanding, the subsequent *I–V* loop after the initial loop (shown in Figure 3a) is shown in Figure 4a and b. When the subsequent positive bias is applied, the oxygen vacancies are gathered to the left Au electrode, resulting in the transition from LRS to HRS. Consequently, the transformation of unipolar to the bipolar MS properties could be completed. Such extraordinary RS behaviors also were reported in ZnO thin film.[41] Besides, it should be mentioned that the slope of $I-V$ curve of the first loop is different between the two LRS in Figure 3a. For the second sweeping loop, as shown in Figure 4a, the slopes are same in the two scanning ranges of LRS. This is because in the second sweeping loop, the unipolar RS has been completely switched into bipolar RS.

The retention and endurance performance of the device are measured. The device shows good retention performance in a period of more than 4000 s, as shown in Figure 4c. At the read voltage of 0.1 V, the RS ratio can be retained to $\sim 10^2$ without any deterioration or HRS/LRS data overlap. Besides, endurance performance is measured to estimate the cycle-to-cycle stability and reproducibility of the memristor. The device is measured under the repetitive pulses with duration of 0.1 s and magnitude of 5V for RESET voltage and – 5 V for SET voltage, as shown in Figure 4d. The resistance at the HRS and LRS is recorded at the read voltage of 0.1 V. The HRS and LRS can be maintained with the RS ratio maintained up to 10^2 for more than 500 repetitive cycles, suggesting good stability and reproducibility of the device. Although the current ON/OFF ratios shown in the $I-V$ loops of Figure 3 b and Figure 4b are more than 10^2, the retention and endurance performance suggest stability and reliability of the 1D MoO_3 nanowires for memory applications.

Furthermore, the metal electrodes play an important role in the RS behaviors for the memristors. Thus, Ag electrodes were used to investigate the RS properties of the individual MoO_3 nanobelts. Inspiringly, a transition from non-volatile MS to volatile TS behaviors can be observed simply by changing the electrode from Au to Ag. Figure 5a shows schematic of the lateral RS devices with Ag as electrodes with the $Ag/MoO_3/Ag$ configuration. The device is initially in the HRS and an electroforming process is required, as shown in the inset of Figure 5b. After the electroforming, the device exhibits bidirectional TS characteristics, as shown in Figure 5b and c. To be more specific, the current abruptly increased from 10^{-8} to 10^{-6} A at 3.5 V and keep in the LRS during the positive sweep. In a negative voltage sweep, an almost symmetric loop to the positive one can be observed. The device is in the HRS at initial stage, suggesting the previous LRS can not be maintained when the bias voltage decreases to zero. Thus, the RS device demonstrates the typical bidirectional TS properties with a large ON/OFF current ratio up to 2×10^2 at 3 V and the threshold voltage of ~ 3.5 V. The positive part of I–V curve is re-plotted using double-logarithmic coordinates for further understanding the mechanism of TS behaviors (inset in Figure 5c). At the HRS, by considering the high work function (Φ, ~ 6.86 eV) of MoO_3, utilizing the metal Ag with the work function of 4.26 eV can not work to form the rectifying junction, consisting with the linear I–V curve. At the LRS, the curve initially follows a linear relationship ($I \sim V$). Then, a quadratic behavior ($I \sim V^2$) can be observed at low voltage ($V < 0.3$ V), suggesting the resistance increasing dramatically and the device switching from the LRS into the HRS, inducing the typical TS behaviors. In this case, the change from the LRS to the HRS can be caused by the breakdown of the conductive filaments. Besides, the MoO_3-based TS device demonstrates good stability. As shown in Figure 5d, the device shows 20 repeatable TS loops.

Herein, we achieve the transition from the MS to the TS in single MoO_3 nanobelts by changing the electrodes from the Au to Ag. Actually, the transition between the TS and the MS was previously reported through setting different the I_{cc} to trigger various types of RS.[26, 27] The MS can be obtained by setting a high I_{cc}, while the TS is stimulated by setting a relatively low I_{cc}. It is well known that the oxygen vacancy plays a significant role in the RS behaviors in oxides.[15] Generally, the formation and breakdown of oxygen vacancy conductive filament give rise to the SET and

RESET process, respectively. The oxygen vacancies can be gathered and form the conductive filaments with appropriate Joule heating. On the other hand, with large Joule heating, oxygen vacancies can be reordered and induce the damage of the filaments. For the TS, the real conductive filament of oxygen vacancy can not be formed due to the low current (low Joule heating). In our experiment, the junction barrier between Au and MoO_3 ($\Phi_{MoO3} - \Phi_{Au}$, ~ 1.7 eV) is relatively low compared to that formed by Ag and MoO_3 (~ 2.6 eV). Thus, the contact resistance of Ag/MoO_3 is much larger than that of Au/MoO_3, resulting the low current in both the HRS and LRS when Ag serving as the electrodes. Thus, no real conductive filament of oxygen vacancy can be formed with the low current. In other words, the large contact resistance between Ag and MoO_3 results in the low current, serving as the low I_{cc} to trigger the TS behaviors in MoO_3 nanobelts with Ag as electrodes.

To further confirm the role played by the oxygen vacancy in the RS behaviors, MoO_3 nanobelts were annealed in nitrogen atmosphere (marked as $MoO_3(N_2)$) to achieve higher concentration of oxygen vacancy. Similar to the aforementioned properties of MoO_3 nanobelts annealed in air (marked as MoO_3(air)) with Ag as electrodes, the typical bidirectional TS behaviors can be observed in the Ag/$MoO_3(N_2)$/Ag RS device, as shown in Figure 6a and b. The electroforming voltage (3 V) is relatively low compared to that of the MoO_3 nanobelts annealed in air, as shown in the inset of Figure 6a. As a consequence, the device can achieve the RS loop at very low work voltage of 1 V. In the loop of positive bias scanning of 0 ~1 V, the current rapidly increased from 10^{-8} to 10^{-5} A at about 0.75 V, corresponding to the switching from the HRS to the LRS. The device with relatively low threshold voltage shows similar bidirectional TS loops to the one annealed in air. Meanwhile, the high ON/OFF current ratio up to 3×10^5 at 0.5 V can be achieved in the Ag/$MoO_3(N_2)$/Ag RS devices, which is 3 orders of magnitude higher than the one annealed in air. Thus, the device has high selectivity and can effectively solve the problem of sneak path current crosstalk.

Then, high resolution x-ray photoemission spectroscopy (XPS) measurements was employed to analyze the chemical composition of MoO_3 nanobelts annealed in air and N_2 for further understanding the effects of oxygen vacancy on the RS behaviors. As shown in Figures 7a for the MoO_3 nanobelts annealed in air, the Mo3d spectrum presents the Mo3$d_{5/2}$ and Mo3$d_{3/2}$ spin-orbit split which are associated with a single oxidation state in MoO_3.[42] Through fitting analysis, the spectrum shows the presence of two types of different molybdenum oxides. To be more specific, the binding energies located at 233.04 eV and 236.18 eV correspond to Mo3$d_{5/2}$ and Mo3$d_{3/2}$, respectively, corresponding to the oxidation state of Mo^{6+}.[43,44] On the other hand, the relatively weak peaks at 231.95 eV and 235.55 eV are respectively assigned to Mo3$d_{5/2}$ and Mo3$d_{3/2}$ for the oxidation state of Mo^{5+}.[45] The concentrations of the multiple oxidation states of Mo^{6+} and Mo^{5+} are 87.4% and 12.5%, respectively. The observation of Mo^{5+} suggests the existence of the oxygen vacancy. Moreover, The O1s spectrum for the MoO_3 annealed in air is shown in Figure 7b. The binding energy located at 532.01 eV corresponds to the oxygen vacancy. According to the XPS spectra, the Mo:O ratio can be calculated to be about 1:2.84, which is close to the chemical composition of the MoO_3. The Mo3d and O1s XPS spectra for $MoO_3(N_2)$ are shown in Figure 7c and d, respectively. The peaks at 231.81 eV and 235.32 eV are assigned to Mo^{5+}, and its concentration is 23.70%. Besides, the weak peaks of Mo^{4+} located at 229.80 eV and 232.62 eV can be detected for the $MoO_3(N_2)$ sample. Furthermore, in Figure 7d, the peak located at about 520 eV corresponding to oxygen vacancy is slightly enhanced compared to that in Figure 7b, suggesting the increased concentration of oxygen vacancy for $MoO_3(N_2)$. The reduction of Mo atoms from the +6 state to the +5 and +4 state in MoO_3, indicating that a large number of oxygen vacancies are introduced by annealing under N_2 atmosphere.[36] The Mo:O ratio can be calculated to be about 1:2.64. The increased concentration of oxygen vacancies plays a vital role in the RS device, giving rise to the observed improved TS behaviors in 1D MoO_3 nanobelts.

EXPERIMENTAL SECTION

Synthesis of MoO_3 nanobelts

The layered MoO_3 nanobelts were synthesized by a hydrothermal method. $(NH_4)_6Mo_7O_{24}\cdot 4H_2O$ (Adamas, G.R. grade, 99.0%$^+$) was served as the source of molybdenum. In a detailed process, 1.24 g $(NH_4)_6Mo_7O_{24}\cdot 4H_2O$ was dissolved into 30 mL distilled water and 1.011 g KNO_3 (Adamas, A.R. grade, 99.0%$^+$) was dissolved into 20 mL of distilled water. At room temperature, the $(NH_4)_6Mo_7O_{24}\cdot 4H_2O$ solution was slowly added into nitrates solution and stirred vigorously until homogeneous solution was formed. The solution pH was adjusted to 1-3 by HNO_3 solution. The obtained clear solution was transferred into 100 mL Teflon-lined stainless autoclave and reacted at 180 °C for 36 h in the oven, then cooled to room temperature naturally. The white precipitate was collected and washed for several times with distilled water by filtration at 8000 rpm, and dried in the a vacuum oven at 60 °C for 12 h. The collected powders were transferred to a crucible, then annealed at 500 °C at a rate of 5 °C/min in air for 2 h. As a comparison, the powders were annealed at 500 °C at a rate of 5 °C/min in N_2 for 2 h.

Characterizations

High resolution XRD (Rigaku XRD, Intelligent Laboratories, Japan) and field emission SEM (FE-SEM, JSM-7500, JEOL, Japan) were used to characterize the crystal structure and surface morphology of the prepared nanobelts. AFM (DI Nanoscope 8) was employed to determine the thickness of the individual nanobelt. Furthermore, the microstructure and morphology of the nanobelts were analyzed by TEM (FE-TEM, GZF20, JEOL, Japan). Energy Dispersive Spectrometer (EDS) was conducted to study the element ratio (JSM-7500, JEOL, Japan). The samples were analyzed by a Raman spectrometer (Renishaw RM2000, UK) with the laser wavelength of 532 nm. Besides, the nanobelts were also characterized by a PHI 5000 Versa Probe XPS instrument (XPS, ESCALAB 250XI, Thermo Fisher, USA) with monochromatic Al-Kα radiation. The C1s peak (located at 284.8 eV) was used to calibrate all the observed the binding energies. All characterizations were performed at room temperature.

Device fabrication and measurements

The Ag/MoO_3/Ag RS devices were fabricated by the a “dry” transferring approach by using the scotch tape to avoid chemical contamination. The individual MoO_3 nanobelts can be transferred from their powder onto SiO_2 substrates through mechanical exfoliation method. Ag and Au electrodes were fabricated with a stripe mask by using sputtering method. The thickness of electrodes is well controlled to be ~100 nm and the distance between the adjacent electrodes is ~30 μm. The adjacent electrodes and the underlying MoO_3 nanobelt can form metal-RS layer-metal configuration for RS measurements. All electrical measurements were performed using a dual channel Keithley 2636B Source Meter with a four-probe station system. The laboratory humidity was well controlled to be 40% to 60%. All the measurements were carried out at room temperature in air.

CONCLUSIONS

We synthesized layered α-MoO_3 nanobelts by hydrothermal method followed by annealing under different atmospheres to adjust the concentration of oxygen vacancies. The prepared single MoO_3 nanobelt is used to serve as the RS layer to construct the lateral two-terminal RS devices. By using

Au as the electrodes, the MoO_3 nanobelts show the typical nonvolatile bipolar MS behaviors, while bidirectional TS properties can be achieved by employing Ag as the electrodes. The transition from the nonvolatile MS to the volatile TS can be achieved simply by changing the electrodes from Au to Ag. The relatively large contact resistance between Ag and MoO_3 nanobelts can be used to address the observed transition between two different RS behaviors. Besides, the threshold RS performance is significantly enhanced with the ON/OFF current ratio increased up to 3×10^5 while the threshold voltage decreased down to 0.75 V by annealing the nanobelts in N_2. This provides us a new way to the development of electronic components by adjusting the defects/vacancies and the selection of electrodes for multifunctional high-performance emerging devices.

Conflicts of interest

There are no conflicts to declare

ACKNOWLEDGEMENTS

This work was supported by the grants from National Natural Science Foundation of China (No. 61604100, No. 61804023, No. 61971108, and No. 61974097), National Students' Platform for Innovation and Entrepreneurship Training Program (201810636090), the Open Foundation of State Key Laboratory of Electronic Thin Films and Integrated Devices (KFJJ201805), Sichuan Youth Science and Technology Foundation (19JCQN0106), Key R&D Program of Sichuan Province (No. 2018GZ0527) and Hong Kong RGC GRF (No. PolyU 153033/17P).

REFERENCES

1. C.-F. Kang, W.-C. Kuo, W. Bao, C.-H. Ho, C.-W. Huang, W.-W. Wu, Y.-H. Chu, J.-Y. Juang, S. H. Tseng, L. Hu and J.-H. He, *Nano Energy*, 2015, **13**, 283-290.
2. P.-H. Liu, C.-C. Lin, A. Manekkathodi and L.-J. Chen, *Nano Energy*, 2015, **15**, 362-368.
3. X. Guan, W. Hu, M. A. Haque, N. Wei, Z. Liu, A. Chen and T. Wu, *Adv. Funct. Mater.*, 2018, **28**, 1704665.
4. Y. Xu, J. Yuan, K. Zhang, Y. Hou, Q. Sun, Y. Yao, S. Li, Q. Bao, H. Zhang and Y. Zhang, *Adv. Funct. Mater.*, 2017, **27**, 1702211.
5. V. K. Sangwan, H. S. Lee, H. Bergeron, I. Balla, M. E. Beck, K. S. Chen and M. C. Hersam, *Nature*, 2018, **554**, 500-504.
6. Y. Sun, X. Yan, X. Zheng, Y. Liu, Y. Zhao, Y. Shen, Q. Liao and Y. Zhang, *ACS Appl. Mater. Interfaces*, 2015, **7**, 7382-7388.
7. Y. Yang, H. Du, Q. Xue, X. Wei, Z. Yang, C. Xu, D. Lin, W. Jie and J. Hao, *Nano Energy*, 2019, **57**, 566-573.

8 Z. Yang, Z. Wu, Y. Lyu and J. Hao, *InfoMat*, 2019, **1**, 98–107.

9 X. Zhao, Z. Wang, Y. Xie, H. Xu, J. Zhu, X. Zhang, W. Liu, G. Yang, J. Ma and Y. Liu, *Small*, 2018, **14**, 1801325.

10. C. Cagli, F. Nardi, B. Harteneck, Z. Tan, Y. Zhang and D. Ielmini, *Small*, 2011, **7**, 2899-2905.
11. M. Xiao, K. P. Musselman, W. W. Duley and Y. N. Zhou, *ACS Appl. Mater. Interfaces*, 2017, **9**, 4808-4817.
12. A. Bera, H. Peng, J. Lourembam, Y. Shen, X. W. Sun and T. Wu, *Adv. Funct. Mater.*, 2013, **23**, 4977-4984.
13. F. M. Simanjuntak, D. Panda, K. H. Wei and T. Y. Tseng, *Nanoscale Res. Lett.*, 2016, **11**, 368.
14. J. Song, Y. Zhang, C. Xu, W. Wu and Z. L. Wang, *Nano Lett.*, 2011, **11**, 2829-2834.
15. K. D. Liang, C. H. Huang, C. C. Lai, J. S. Huang, H. W. Tsai, Y. C. Wang, Y. C. Shih, M. T. Chang, S. C. Lo and Y. L. Chueh, *ACS Appl. Mater. Interfaces*, 2014, **6**, 16537-16544.
16. W. Wu and Z. L. Wang, *Nano Lett.*, 2011, **11**, 2779-2785.
17. C. W. Hsu and L. J. Chou, *Nano Lett.*, 2012, **12**, 4247-4253.
18. L. Cai, C. J. McClellan, A. L. Koh, H. Li, E. Yalon, E. Pop and X. Zheng, *Nano Lett.*, 2017, **17**, 3854-3861.
19. M. Kröger, S. Hamwi, J. Meyer, T. Riedl, W. Kowalsky and A. Kahn, *Appl. Phys. Lett.*, 2009, **95**, 123301.
20. Y. Guo and J. Robertson, *Appl. Phys. Lett.*, 2014, **105**, 222110.
21. Z.-H. Tan, X.-B. Yin and X. Guo, *Appl. Phys. Lett.*, 2015, **106**, 023503.
22. L. Cario, C. Vaju, B. Corraze, V. Guiot and E. Janod, *Adv. Mater.*, 2010, **22**, 5193-5197.
23. A. Q. Jiang, C. Wang, K. J. Jin, X. B. Liu, J. F. Scott, C. S. Hwang, T. A. Tang, H. B. Lu and G. Z. Yang, *Adv. Mater.*, 2011, **23**, 1277-1281.
24. E. J. Yoo, M. Lyu, J. H. Yun, C. J. Kang, Y. J. Choi and L. Wang, *Adv. Mater.*, 2015, **27**, 6170-6175.

25 X. Zhao, H. Xu, Z. Wang, Y. Lin and Y. Liu, *InfoMat*, 2019, **1**, 183–210.

26. H. Wang, Y. Du, Y. Li, B. Zhu, W. R. Leow, Y. Li, J. Pan, T. Wu and X. Chen, *Adv. Funct. Mater.*, 2015, **25**, 3825-3831.
27. H. Sun, Q. Liu, C. Li, S. Long, H. Lv, C. Bi, Z. Huo, L. Li and M. Liu, *Adv. Funct. Mater.*, 2014, **24**, 5679-5686.
28. R. Midya, Z. Wang, J. Zhang, S. E. Savel'ev, C. Li, M. Rao, M. H. Jang, S. Joshi, H. Jiang, P. Lin, K.

Norris, N. Ge, Q. Wu, M. Barnell, Z. Li, H. L. Xin, R. S. Williams, Q. Xia and J. J. Yang, *Adv. Mater.*, 2017, **29**, 1604457.

29. Y. Sun, X. Zhao, C. Song, K. Xu, Y. Xi, J. Yin, Z. Wang, X. Zhou, X. Chen, G. Shi, H. Lv, Q. Liu, F. Zeng, X. Zhong, H. Wu, M. Liu and F. Pan, *Adv. Funct. Mater.*, 2019, **29**, 1808376.
30. C. Zhang, J. Shang, W. Xue, H. Tan, L. Pan, X. Yang, S. Guo, J. Hao, G. Liu and R. W. Li, *Chem. Commun.*, 2016, **52**, 4828-4831.
31. L. He, Z. M. Liao, H. C. Wu, X. X. Tian, D. S. Xu, G. L. Cross, G. S. Duesberg, I. V. Shvets and D. P. Yu, *Nano Lett.*, 2011, **11**, 4601-4606.

32 X. Zhao, Z. Fan, H. Xu, Z. Wang, J. Xu, J. Ma and Y. Liu, *J. Mater. Chem. C*, 2018, **6**, 7195–7200.

33 X. Zhao, H. Xu, Z. Wang, L. Zhang, J. Ma and Y. Liu, *Carbon N. Y.*, 2015, **91**, 38–44.

34. K. Kalantar-zadeh, J. Tang, M. Wang, K. L. Wang, A. Shailos, K. Galatsis, R. Kojima, V. Strong, A. Lech, W. Wlodarski and R. B. Kaner, *Nanoscale*, 2010, **2**, 429-433.
35. D. D. Yao, J. Z. Ou, K. Latham, S. Zhuiykov, A. P. O'Mullane and K. Kalantar-zadeh, *Cryst. Growth Des.*, 2012, **12**, 1865-1870.
36. Q. P. Ding, H. B. Huang, J. H. Duan, J. F. Gong, S. G. Yang, X. N. Zhao and Y. W. Du, *J. Cryst. Growth Des.*, 2006, **294**, 304-308.
37. M. M. Alsaif, K. Latham, M. R. Field, D. D. Yao, N. V. Medhekar, G. A. Beane, R. B. Kaner, S. P. Russo, J. Z. Ou and K. Kalantar-zadeh, *Adv. Mater.*, 2014, **26**, 3931-3937.

38 R. Moo, S. Balendhran, S. Walia, M. Alsaif, E. P. Nguyen and J. Z. Ou, *ACS Nano*, 2013, 7, 9753–9760.

39 S. Balendhran, J. Deng, J. Z. Ou, S. Walia, J. Scott, J. Tang, K. L. Wang, M. R. Field, S. Russo, S. Zhuiykov, M. S. Strano, N. Medhekar, S. Sriram, M. Bhaskaran and K. Kalantar-Zadeh, *Adv. Mater.*, 2013, **25**, 109–114.

40 G. Milano, S. Porro, I. Valov and C. Ricciardi, *Adv. Electron. Mater.*, 2019, 1800909.

41 C. Huang, J. Huang, C. Lai, H. Huang, S. Lin and Y. Chueh, *ACS Appl. Mater. Interfaces*, 2013, **5**, 6017−6023.

42. F. Rahman, T. Ahmed, S. Walia, E. Mayes, S. Sriram, M. Bhaskaran and S. Balendhran, *Nanoscale*, 2018, **10**, 19711-19719.
43. J. Baltrusaitis, B. Mendoza-Sanchez, V. Fernandez, R. Veenstra, N. Dukstiene, A. Roberts and N. Fairley, *Appl. Surf. Sci.*, 2015, **326**, 151-161.
44. S. S. Sunu, E. Prabhu, V. Jayaraman, K. I. Gnanasekar, T. K. Seshagiri and T. Gnanasekaran, *Sensor. Actuat. B-Chem.*, 2004, **101**, 161-174.
45. S. Yang, Z. Wang, Y. Hu, Y. Cai, R. Huang, X. Li, Z. Huang, Z. Lan, W. Chen and H. Gu, *Sensor. Actuat. B-Chem.*, 2018, **260**, 21-32.

Figures

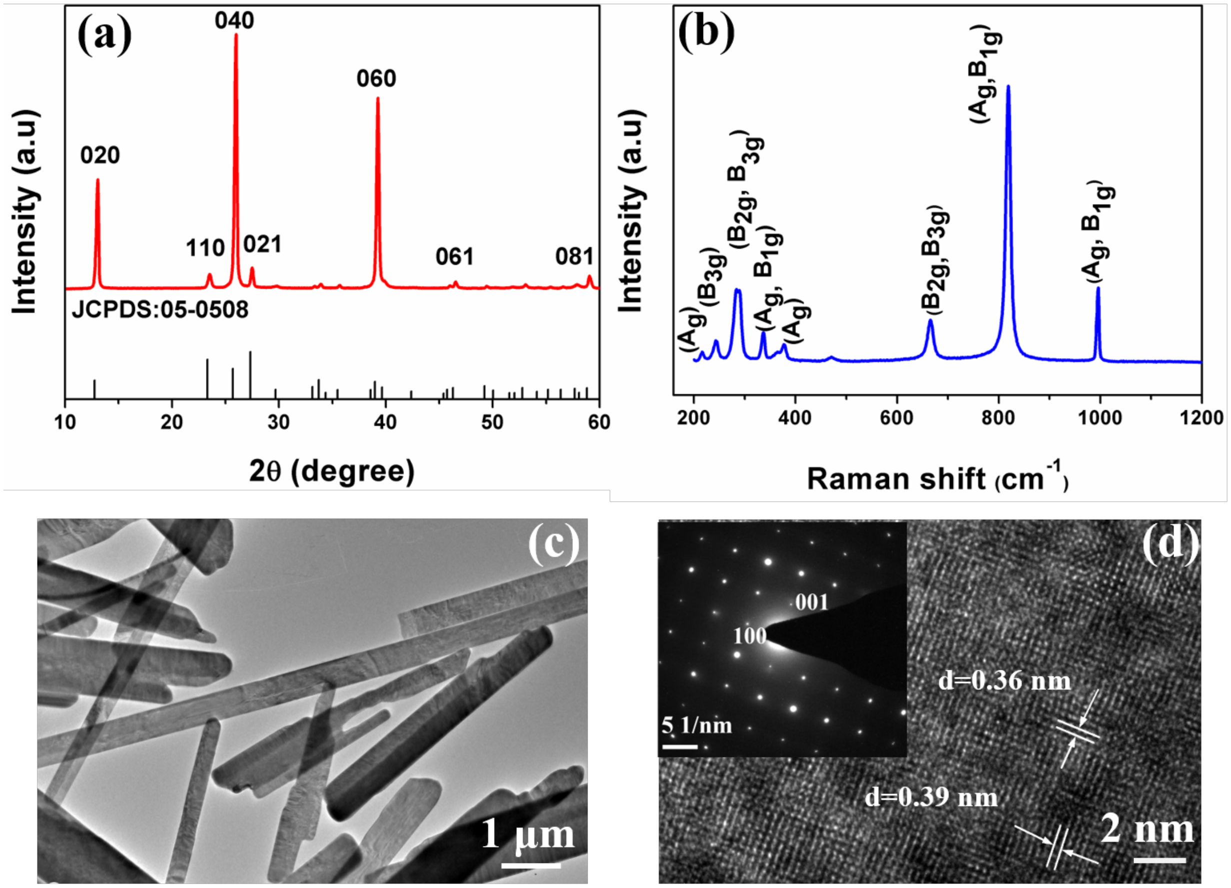

Figure 1. (a) Powder XRD pattern of the as-prepared MoO_3 nanobelts. The standard pattern of the MoO_3 phase is shown in the bottom. (b) Raman spectrum of the MoO_3 nanobelts. (c) TEM image of the MoO_3 nanobelts. (d) HRTEM image of the MoO_3 nanobelts. The inset shows the selected area electron diffraction pattern.

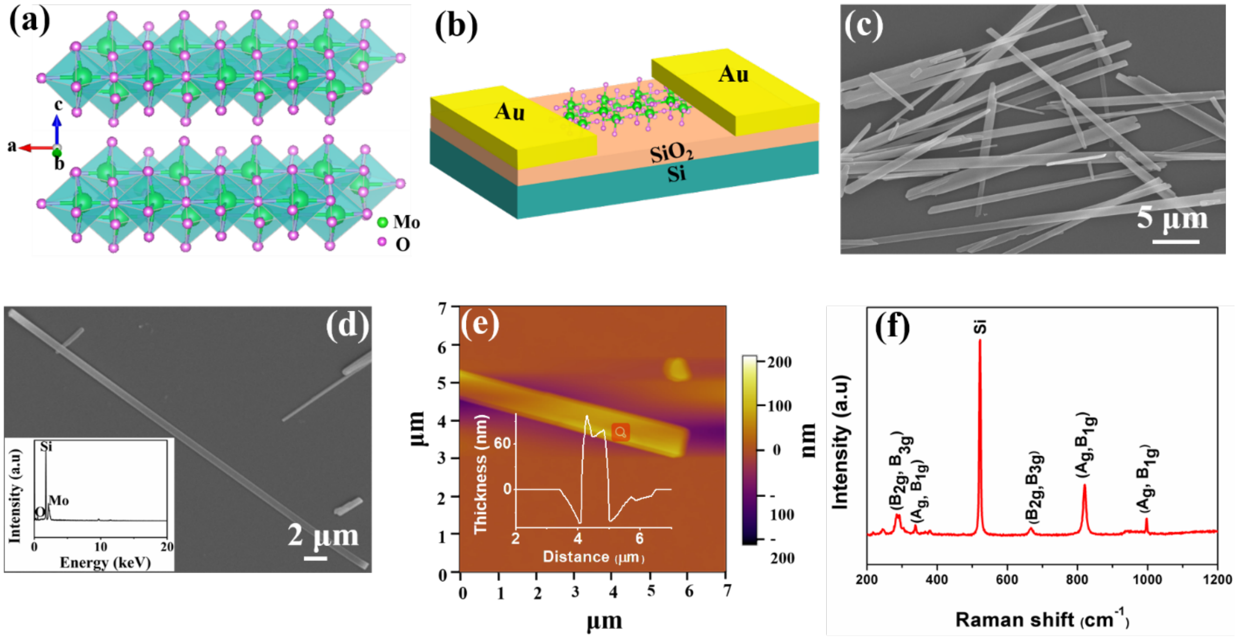

Figure 2. (a) α-MoO_3 structure composed of edge sharing double layers of MoO_6 octahedra. (b) Schematic of the fabricated RS device with the Au/MoO_3/Au configuration. (c) SEM image of the as-prepared MoO_3 nanobelts on the SiO_2/Si substrate. (d) SEM image of an individual MoO_3 nanobelt on the Si/SiO_2 substrate. The inset shows the EDX image (Mo : O about 1:3). (e) AFM image of an individual MoO_3 nanobelt. (f) Raman spectrum of an individual MoO_3 nanobelt on Si/SiO_2 substrate.

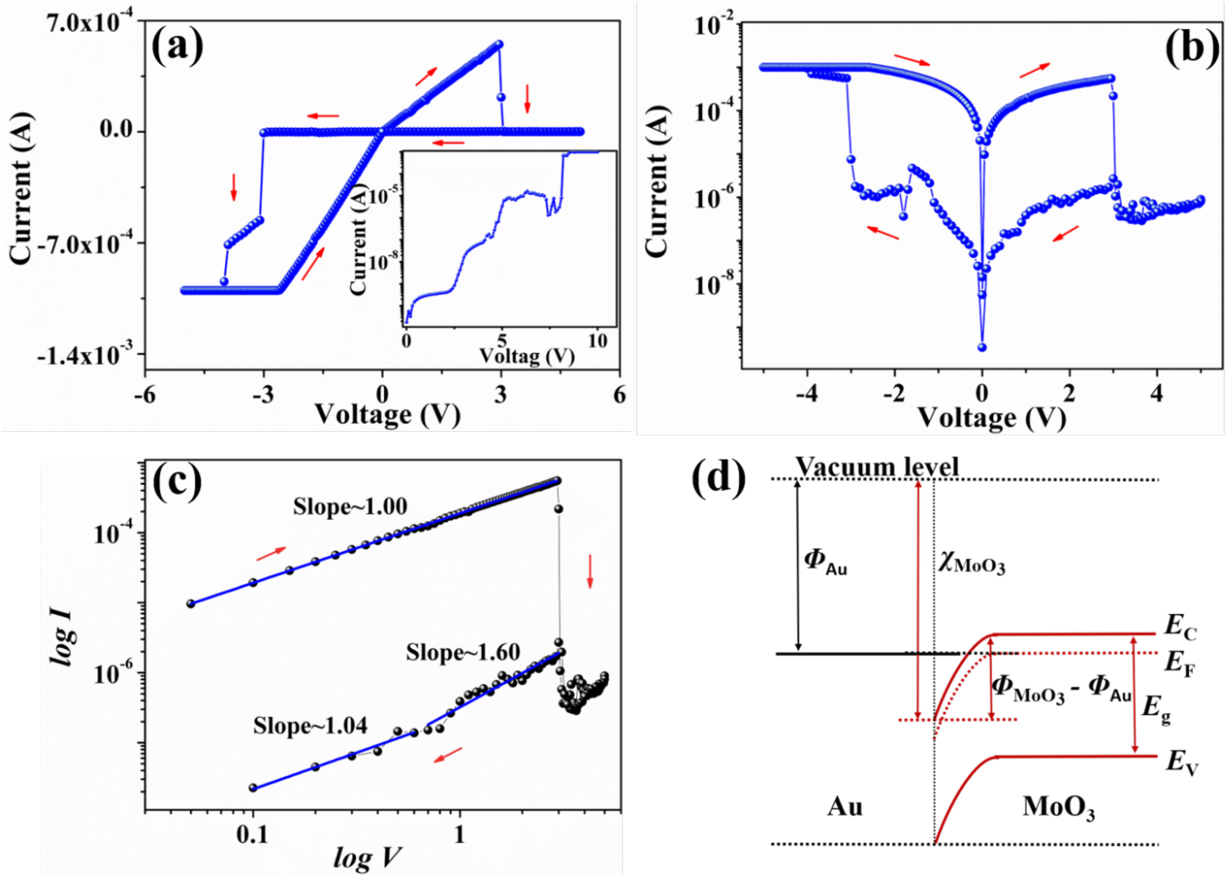

Figure 3. MS behaviors of the MoO_3 nanobelt with Au as electrode. $I-V$ curve in (a) linear scale and (b) logarithmic scale. The inset in (a) shows a forming process of the device. (c) The positive part of the $I-V$ curve in (b) is re-plotted in a double-logarithmic coordinate and linear fitting of $log\ I-log\ V$ curve. (d) Schematic of electronic band structure of the junction between metal Au and semiconducting MoO_3. E_C, E_V, E_F and E_g represent the conduction band edge, the valence band edge, the Fermi level and the band gap of MoO_3, respectively.

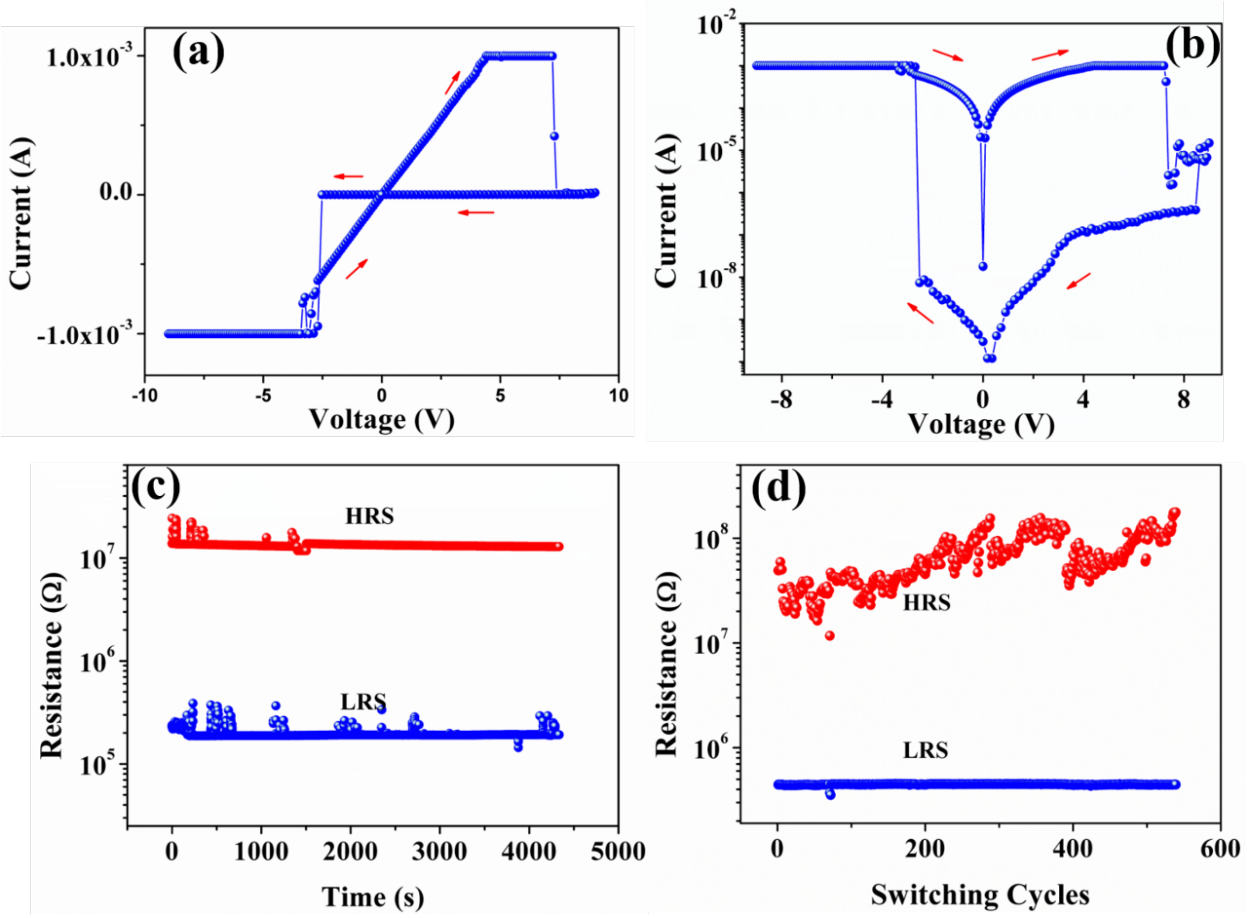

Figure 4. MS behaviors of the MoO_3 nanobelt with Au as electrode. The second $I-V$ loop of the in (a) linear scale and (b) logarithmic scale. (c) Retention of the HRS and LRS as function of time. (d) Performance endurance as a function of switching cycles.

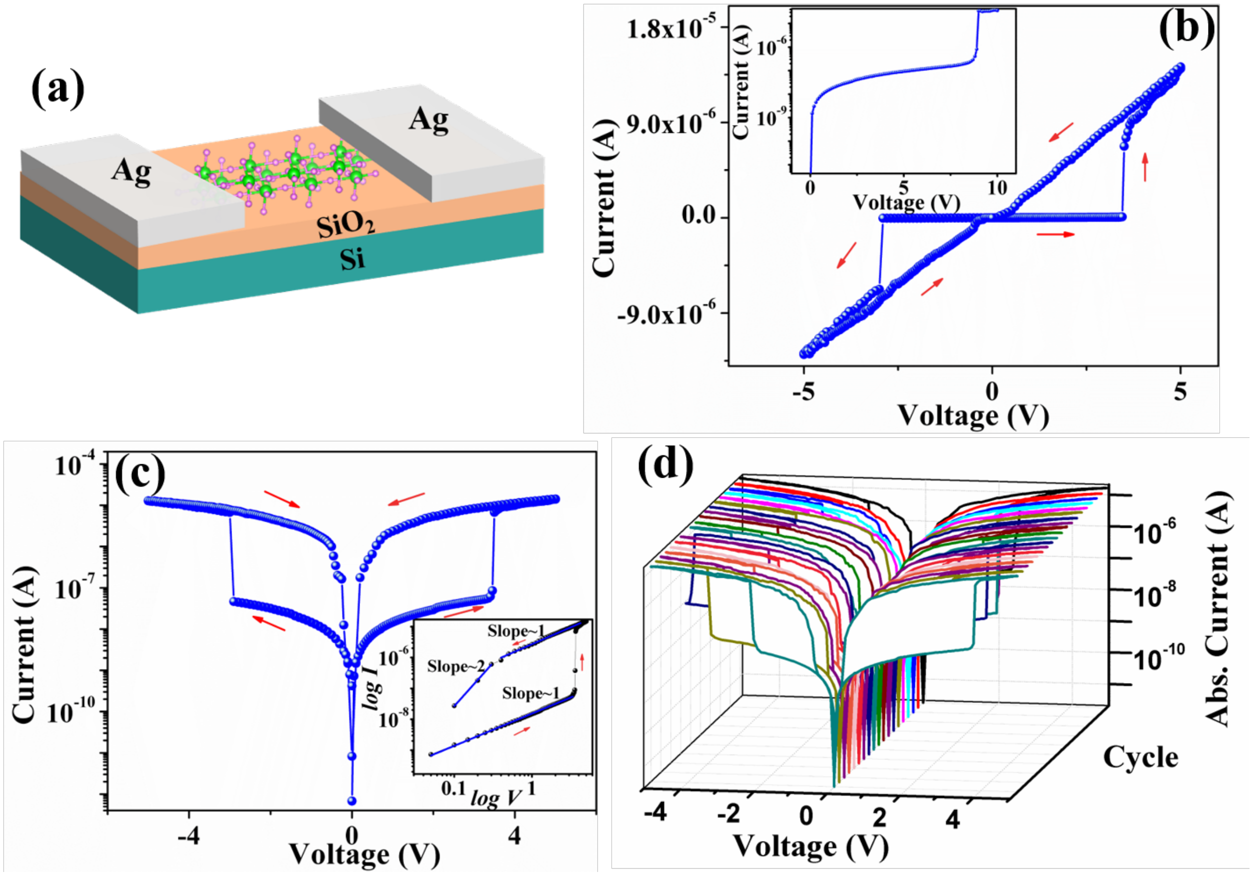

Figure 5. TS behaviors of the MoO_3 nanobelt with Ag as electrode. (a) Schematic of the fabricated TS device. $I-V$ curve in (b) linear scale and (c) logarithmic scale. The inset shows the positive part of the $I-V$ curve in (c) re-plotted in a double-logarithmic coordinate and linear fitting of $log\ I-log\ V$ curve. (d) 20 experimental switching circles.

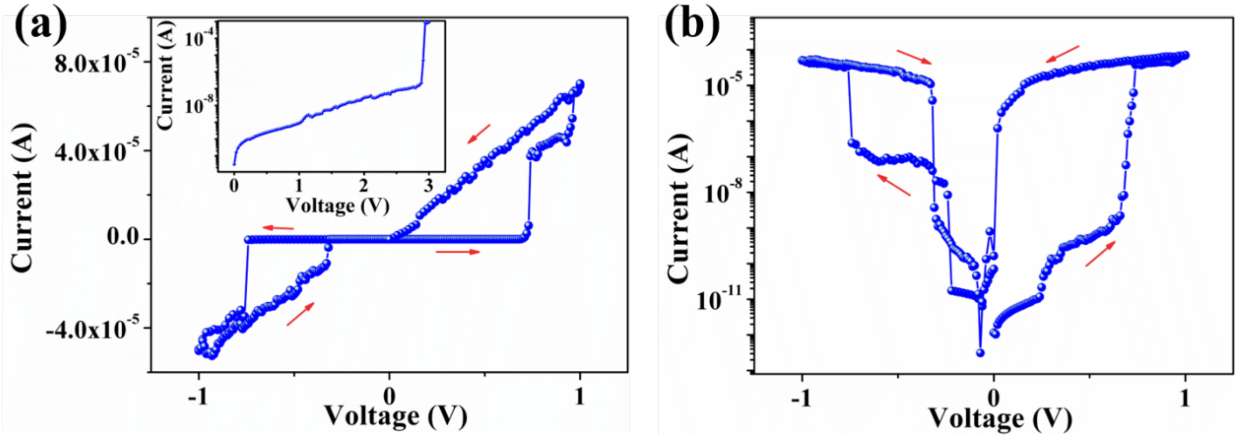

Figure 6. TS behaviors of the $MoO_3(N_2)$ nanobelt with Ag as electrode. $I-V$ curve in (a) linear scale and (b) logarithmic scale. The inset in (a) shows a forming process of the device.

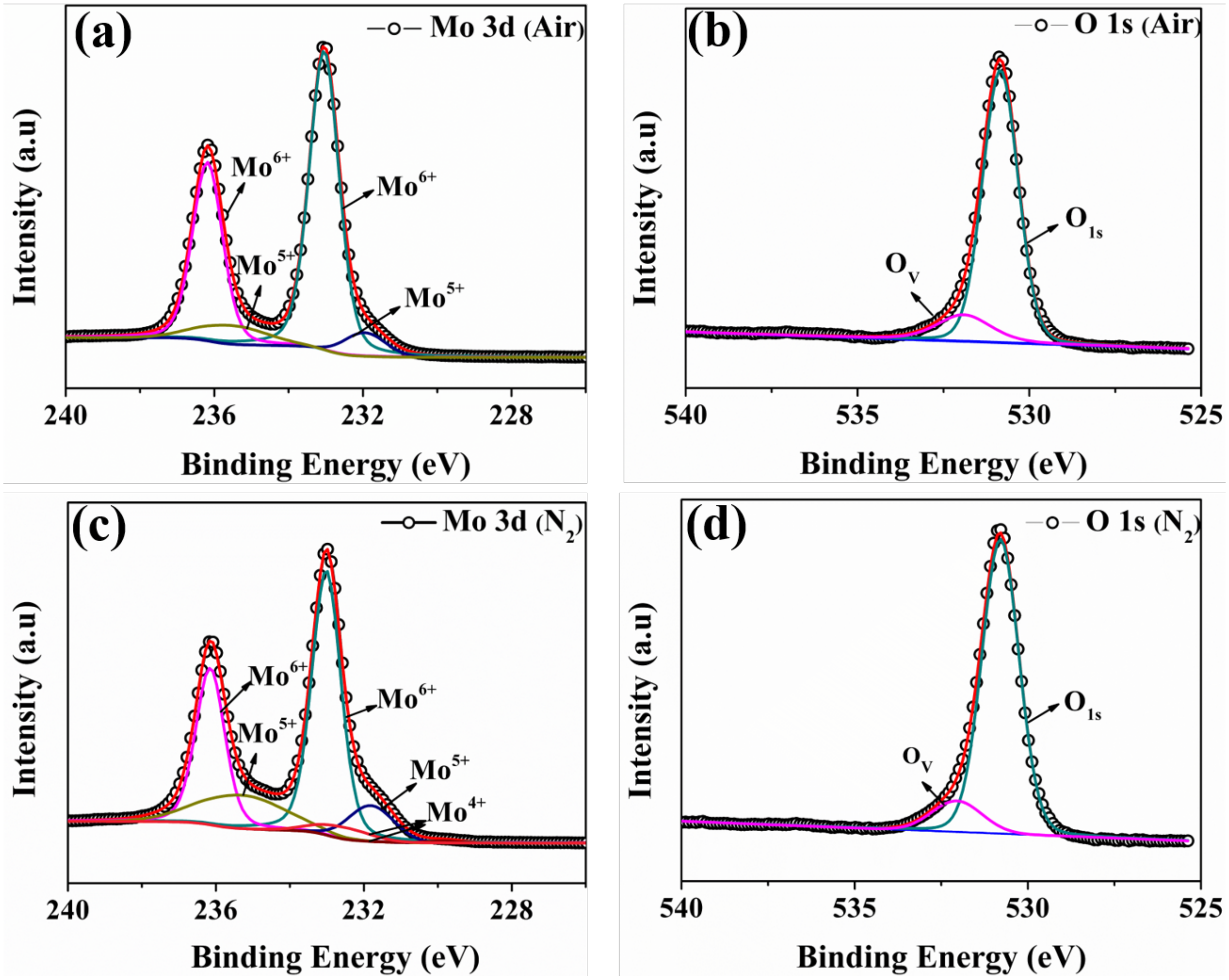

Figure 7. The XPS results of the prepared MoO_3 nanobelts. The fitted XPS spectrum of Mo 3d core level (a) and (b) O 1s core level for MoO_3 nanobelts annealed in air. The fitted XPS spectrum of Mo 3d core level (c) and (d) O 1s core level for MoO_3 nanobelts annealed in N_2.